Dalton
Transactions

PAPER

View Article Online
View Journal | View Issue

Cite this: *Dalton Trans.*, 2025, **54**, 17814

High-nuclearity Cu hydride nanoclusters of $Cu_{22}H_{19}$ and $Cu_{20}H_{13}$ consolidated by an N-containing triphosphine ligand: synthesis, characterization and catalysis

Meng-Xia Ma,†[a,c] Yi-Wu Zhou, †[a] Zi-Jian Gui,[a] Ting-Hong Huang, *[b] Qing-Ling Ni,[a] Shi-Ming Li,[a] Liu-Cheng Gui*[a] and Xiu-Jian Wang *[a]

Received 2nd October 2025,
Accepted 5th November 2025

DOI: 10.1039/d5dt02358k

rsc.li/dalton

The synthesis of copper hydride nanoclusters and the determination of their atomically precise structures are beneficial for gaining an in-depth understanding of the structure–property relationship. N,P-containing ligands with a combination of hard and soft donors exhibit versatile coordination modes which are promising for mediating the structures of Cu hydride nanoclusters and their properties. Herein, two Cu hydride nanoclusters, $[Cu_{22}H_{19}(NP_3)_4(CH_3CN)_4]\cdot(ClO_4)_3$ (**1**) and $[Cu_{20}H_{13}(NP_3)_4(CH_3CN)_3Cl_4]\cdot(ClO_4)_3$ (**2**), based on the tripodal N-containing triphosphine ligand of tris(diphenylphosphino-ethyl)amine (NP_3) are synthesized, and their compositions and structures are determined by ^1H NMR, high-resolution ESI-MS and single-crystal X-ray diffraction. The location of hydrides is established based on the optimized model obtained by DFT calculations. In cluster **1**, the skeleton of 22 Cu can be described as a fusion of two distorted Cu_{13} centred icosahedra by sharing four Cu atoms, and each NP_3 ligand exhibits a tridentate mode (P, P, P) to bind one Cu_3 triangular plane. The skeleton of 20 Cu in cluster **2** can be described as a Cu_{13} centred icosahedron bridging a cap-shaped Cu_7 moiety, and the ligands exhibit two binding modes, the tridentate (P, P, P) and the tetradentate (N, P, P, P) modes, to consolidate these Cu atoms. The synthesis of clusters **1** and **2** is similar. The involvement of Cl^- anions and the flexibility of NP_3 play a synergistic role in mediating the construction of cluster **2**, resulting in a structure distinct from that of cluster **1**. Their deuteride analogues, $\mathbf{1}_D$ and $\mathbf{2}_D$, are also synthesized for comparison. Cluster **2** exhibits better catalytic activity than cluster **1** for the reduction of 4-nitrophenol to 4-aminophenol.

Introduction

The study of monodisperse and atomically precise coinage metal (Au, Ag, Cu and their alloys) nanoclusters protected by organic ligands has attracted continuing attention, not only because of their aesthetically pleasing molecular structures and interesting properties, but also as it allows for the development of direct structure–property relationships of nanoclusters.[1–13] Through tremendous efforts over the past few decades, a large number of nanoclusters containing from a few tens to hundreds metal atoms have been synthesized and their structures atom-precisely determined.[14–22] The detailed structural anatomy of nanoclusters can seek to understand the kernel structures and the growth mode of kernels, the surface structures and the self-assembly of surface protecting ligands, as well as the interfacial bonding between the kernel and the surface structure.[23–27] The observed growth modes of kernels in nanoclusters include kernel fusion, interpenetration, cluster of cluster, shell by shell, and layer by layer.[28,29] The peripheral ligands and the assembled metal–ligand motifs (termed as staple motifs) govern a nanocluster's stability and geometric and electronic structures. For example, the surface ligands in Au_{247} induce nanocluster hierarchical self-assembly into complex structures,[25] and the clockwise/anticlockwise configuration of $Au_n(SR)_{n+1}$ bonds in Au_{38}(2-PET)$_{24}$ (2-PET: 2-phenylethylthiolate) creates a pair of enantiomers.[30] $M_n(SR)_{n+1}$ (M = Au and Ag) bonds are commonly observed in nanoclusters, and their flexibility and diversity contribute to various nanoclusters.[31–33] Moreover, metal-alkynyl and mixed P–metal–S–metal–P bonds are also reported with various configurations to anchor the kernel of nanoclusters for structural stability.[34] As is well known, systematic

---

[a] *School of Chemistry and Pharmaceutical Sciences, Guangxi Normal University, Guilin 541004, China. E-mail: wang1_xj@aliyun.com, guiliucheng2000@163.com*
[b] *School of Chemical Engineering, Sichuan University of Science & Engineering, Zigong, 643000, China. E-mail: hth_chem@126.com*
[c] *School of Laboratory Medicine, Youjiang Medical University for Nationalities, Baise, 533000 Guangxi, PR China*

† These authors contributed equally.

studies of nanoclusters can establish the structure–property relations.

Though a large number of atom-precise Cu nanoclusters have been reported, the metastability of Cu nanoclusters resulting from their high susceptibility towards oxidation,[35–37] to a certain degree, prevents systematic comparative studies. Among the family of Cu clusters, Cu hydride nanoclusters have attracted special attention since they are key intermediates in numerous copper-catalyzed reactions and promising materials for hydrogen storage.[38–43] Some successful synthetic protocols have been established for the preparation of copper hydride nanoclusters based on stabilizing reagents such as thiolates, selenide, phosphines, dithiophosphate, dithiocarbamates, or their combinations. But only a handful of copper hydride nanoclusters with more than 20 Cu atoms have been reported with atomically precise structures, including $Cu_{20}H_{11}$,[44] $Cu_{23}H_6$,[45] $Cu_{25}H_{10}$,[46] $Cu_{25}H_{22}$,[47] $Cu_{26}H_{11}$,[48] $Cu_{28}H_8$,[49] $Cu_{28}H_{10}$,[50] $Cu_{28}H_{15}$,[33] $Cu_{28}H_{16}$,[51] $Cu_{28}H_{20}$,[52] $Cu_{29}H_{22}$,[53] $Cu_{30}H_{18}$,[54] $Cu_{31}H_6$,[55] $Cu_{32}H_8$,[56] $Cu_{32}H_{20}$,[57] $Cu_{36}H_{10}$,[58] $Cu_{40}H_{38}$,[59] $Cu_{41}H_{25}$,[60] $Cu_{53}H_{18}$,[61] $Cu_{57}H_{20}$,[62] $Cu_{58}H_{20}$,[63,64] $Cu_{61}H_{14}$,[65] $Cu_{70}H_{22}$ [66] and $Cu_{81}H_{32}$.[67] Unlike thiolates and alkynes having variable coordination modes, neutral phosphine ligands just terminally coordinate to metal atoms and have, to a certain extent, predetermined steric configurations.[68–70] Therefore, a phosphine ligand with definite coordination mode can be an appropriate candidate to regulate the size and shape of nanoclusters depending on phosphine's steric and size constraint. But the stability of Cu hydride clusters just based on phosphine ligands is a big problem. So phosphine ligands usually perform as auxiliary ligands to construct high-nuclearity nanoclusters.[9,21,45,56,58,71] Hexameric complexes are most common with monodentate phosphine ligands, such as Stryker's reagent, $[(PPh_3)\text{-}CuH]_6$, which is commercially available.[72] To date, only six Cu hydride clusters with more than 10 Cu atoms have been reported just based on phosphine ligands, of which three clusters, $[Cu_{14}H_{12}(phen)_6(PPh_3)_4]^{2+}$,[73] $[Cu_{18}H_{17}(PPh_3)_{10}]^{+}$,[47] and $[Cu_{25}H_{22}(PPh_3)_{12}]^{+}$,[47] are based on monodentate phosphine ligands and three examples, $[Cu_{16}H_{14}(dpmppm)_4]^{2+}$,[74] $[Cu_{16}H_{14}(DPPA)_6]^{2+}$,[76] and $[Cu_{18}H_{16}(DPPE)_6]^{2+}$,[75] are based on polyphosphine ligands. Polyphosphine ligands can also perform as a bonding mode to stabilize metal clusters, similar to $Au(Ag)_n(SR)_{n+1}$. Moreover, polyphosphine ligands with predetermined steric constraints can aggregate metal atoms into clusters with metal–metal bonds. We selected a branched tetradentate ligand, tris(diphenylphosphino-methyl)amine (NP_3), containing three $P(CH_2)N$ sites with a combination of hard and soft donors, to stabilize some Ag nanoclusters: $[Ag_{15}Cl_4(NP_3)_4]^{3+}$,[5] $[Ag_{12}(NP_3)_2(Spz)_{12}]$ and $[Ag_{18}(NP_3)_4(Spz)_{12}]^{6+}$ (Spz = pyrazine-2-thiolate).[76] In the Ag_{15} cluster, each NP_3 ligand performs as a tetradentate mode (N, P, P, P) to participate in coordination, but the central N atom of NP_3 in the Ag_{18} and Ag_{12} clusters does not bond with metal ion where each NP_3 just performs as a tridentate mode (P, P, P). Guan *et al.* used $HN(CH_2CH_2PR_2)_2$ (RPNHP) to construct $[Cu_6H_6(RPNHP)_3]$ and $[Cu_4H_4(RPNHP)_2]$ clusters where the N atom is also uncoordinated, but a mononuclear copper hydride, (RPNHP)CuH, with the NH group bound to copper is proposed as a catalytically active species.[41] Surely in these types of ligands, the hemilabile coordination of hard N atom to soft coinage metal atom will favor cluster transformation, shape/size adjustment and metal surface reaction.

We seek to exploit the bonding coordination mode and the steric confinement of an N-containing polyphosphine ligand to synthesize stable Cu hydride clusters and to regulate their geometric configuration, electronic structures and properties. Herein, the tripodal tetradentate ligand NP_3 is selected as a stabilizing agent for the construction of Cu hydride nanoclusters, due to its geometric flexibility and variable coordination modes. And two nanoclusters, $[Cu_{22}H_{19}(NP_3)_4(CH_3CN)_4](ClO_4)_3$ (**1**) and $[Cu_{20}H_{13}(NP_3)_4(CH_3CN)_3Cl_4](ClO_4)_3$ (**2**), are successfully synthesized and characterized by single-crystal X-ray diffraction, ^1H NMR, and high-resolution electrospray ionization mass spectrometry (HR ESI-MS). There are four NP_3 ligands involved in each of **1** and **2**. However, no N atom from NP_3 ligands participates in coordination in cluster **1**, while only the N atom in one NP_3 ligand does not participate in coordination in cluster **2**.

Results

Synthesis and characterization

Synthetic methods for **1** and **2** are similar (see the experiment part in the SI). The reactions proceeded at 0 °C in a solution of CH_3OH and CH_3CN containing Cu powder, $[Cu(CH_3CN)_4]ClO_4$ and $NaBH_4$ (Scheme 1). The addition of $CuCl_2$ for the preparation of cluster **2** is just to provide a Cl^- source. If Ph_4PCl is used instead of $CuCl_2$, nanocluster **2** can also be afforded with a comparable yield. The hydrides originate from $NaBH_4$. Due to the different sizes of H^- and Cl^- anions, the introduction of Cl^- ions aims to modify the structure of the Cu hydride nanocluster. Interestingly, the presence of Cu powder is crucial for the formation of **1** and **2**, which could be due to Cu powder inhibiting the oxidation of Cu^+ in the reaction process. In the absence of Cu powder, the yields of resulting cluster crystals are much lower, even though the reactions are also carried out under the reducing condition provided by $NaBH_4$. Perhaps the fast reaction between Cu^{2+} ions and Cu powder ensures all Cu species exist as Cu^+ ions in the reactive system, improving the yields of theses clusters. High-quality orange-yellow rhombic crystals of **1** and red cubic crystals of **2** are obtained from a solution with mixed solvents of $MeCN/MeOH/Et_2O$ in a

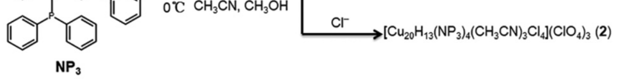

Scheme 1 The synthetic routes to nanoclusters **1** and **2**.

refrigerator at −20 °C (Fig. S1). The UV-visible absorption spectra of the as-obtained nanoclusters **1** and **2** have no dominant visible absorption peaks (Fig. S2), and their time-dependent optical absorption spectra show that they are stable in CH_3CN solvent (Fig. S3). The optical energy gaps were determined to be 2.28 eV for **1** and 2.79 eV for **2** by extrapolating the lowest-energy absorption peak to zero absorbance (see the insets in Fig. S2). The high-resolution XPS spectrum of Cu 2p shows two sharp peaks at binding energies of 932.3 and 952.1 eV for cluster **1**, as well as at 932.8 and 952.7 eV for cluster **2**, which originate from Cu $2p_{3/2}$ and $2p_{1/2}$, respectively, and are similar to those of Cu(I) (Fig. S4).[45,50] Moreover, there is no observable satellite signal at around 943 eV, which indicates the absence of Cu(II) in clusters **1** and **2**. These two clusters are stable in DMSO at low temperature (−20 °C) for longer than three months (Fig. S5). The compositions of clusters **1** and **2** are determined by single-crystal X-ray diffraction, ^{1}H NMR, and HR ESI-MS, and supported by theoretical calculation. To investigate the presence of hydrides, their corresponding deuteride analogues, $\mathbf{1_D}$ and $\mathbf{2_D}$, are also synthesized. The crystal data and structure refinement for **1** and **2** are given in Table S1.

The crystal structure, ESI-MS and ^{1}H NMR for nanocluster 1

Single-crystal X-ray diffraction shows that cluster **1** crystallizes in the triclinic $P\bar{1}$ space group. The asymmetric unit contains a pair of enantiomers of $[Cu_{22}(NP_3)_4(CH_3CN)_4]$ moiety and six ClO_4^- anions, indicating that the electronic charge of cluster **1** would be +3. All NP_3 ligands in an enantiomer exhibit the same conformation, clockwise or anticlockwise (Fig. S6). Below we choose an enantiomer for structural analysis, due to these two enantiomeric pairs showing similarity in their coordination environments. The skeleton of 22 Cu in **1** can be viewed as two fused Cu_{13} centered icosahedra which share four common atoms that construct a twisted quadrilateral, as shown in Fig. 1a. Each icosahedron associates with two NP_3 ligands and two coordinated MeCN molecules. Moreover, each NP_3 ligand adopts a tridentate mode (P, P, P) to bind one Cu_3 triangular plane. The steric effect of the large-sized NP_3 ligand can lead to icosahedra being distorted, resulting in two adjacent Cu_4 quadrilaterals formed at the surface of each distorted Cu_{13} centered icosahedra. The two centred Cu atoms and four fused Cu atoms construct a twisted octahedral Cu_6 core which does not contact any NP_3 and solvent ligands (Fig. 1b). The fusion of icosahedral M_{13} moieties is usually observed for the construction of nanoclusters, such as the vertex-fusion of Au_{13} in $[Au_{37}(PPh_3)_{10}(SR)_{10}Cl_2]^+$ (ref. 77) and $(PtAg_{12})$ in $[Pt_3Ag_{44}\{S_2P\text{-}(OPr)_2\}_{22}]$ (ref. 78)[78] to construct linear structures, Au_{13} in $[Au_{60}Se_2\text{-}(PPh_3)_{10}(SePh)_{15}]^+$ (ref. 79)[79] and $(Au/Ag)_{13}$ in $[(p\text{-}Tol_3P)_{12}Au_{18}\text{-}g_{19}Br_{11}]^+$ (ref. 80)[80] to construct cyclic structures, as well as the fusion of triangular faces of Au_{13} in $Au_{38}(SC_2H_4Ph)_{24}$[30] and in the computational mode of $[Au_{33}(Au_{18}Cl_{30})]^-$,[81] and the interpenetration fusion of Au_{13} in $Au_{30}S(S\text{-}^tBu)_{18}$.[82] The structure of **1** can be also described as that an octahedral Cu_6 core is pocketed by two roof-shaped $[Cu_8(NP_3)_2(CH_3CN)_2]$ units in which eight Cu atoms construct four triangles and two quadrilaterals (Fig. 1b and S7).

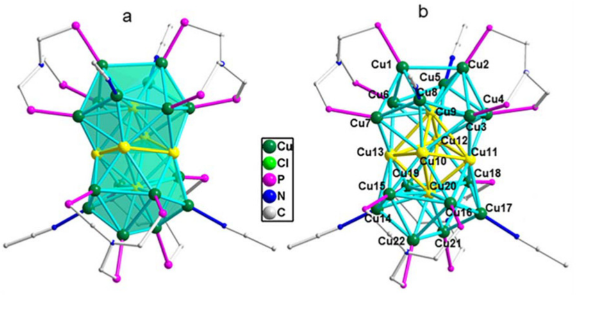

Fig. 1 The crystal structure of cluster **1**. (a) The two centred Cu_{13} fused icosahedra; and (b) the centred octahedron capped by two roof-shaped $[Cu_8(NP_3)_2(CH_3CN)_2]$ units. The centred and fused Cu atoms are labelled in yellow colour. All phenyl groups and hydrogen atoms are omitted for clarity.

The twisting of two fused icosahedra results in the overall conformation of **1** with internal helicity, exhibiting a chiral feature. Both chiral enantiomers crystallize as a racemic mixture. The Cu–Cu distances in **1** are in the range of 2.430(2)–2.883(1) Å, and the average bond lengths of Cu_{center}–Cu_{icos}, Cu_{octa}–Cu_{shell} and Cu_{shell}–Cu_{shell} are 2.595 Å (range: 2.452(3)–2.856(3) Å), 2.533 Å (range: 2.430(2)–2.782(4) Å) and 2.683 Å (range: 2.508(3)–2.883(1) Å), respectively, which are comparable to those found in other Cu hydride clusters.[47] Also, the Cu–P distances (av. 2.263 Å) are typical of those found in Cu(I) phosphine complexes.[41,47,74]

To further determine the composition and charge state of **1**, HR ESI-MS is performed (Fig. S8). The positive mode ESI-MS spectrum of **1** shows two prominent peaks centred at 1287.80 with a charge of +3 and 1981.17 with a charge of +2, which are assigned respectively to the formulas of $[Cu_{22}H_{19}(NP_3)_4]^{3+}$ and $[Cu_{22}H_{19}(NP_3)_4(ClO_4)]^{2+}$ (Fig. 2), while the ESI-MS spectrum of its deuteride analogue, $\mathbf{1_D}$, shows signals centred at 1293.51 with a charge of +3 and 1990.72 with a charge of +2, which correspond respectively to the formulas of $[Cu_{22}D_{16}H_3(NP_3)_4]^{3+}$ and $[Cu_{22}D_{19}(NP_3)_4(ClO_4)]^{2+}$ (Fig. S9). These formula assignments are validated by the good agreement between calculated and experimental isotopic patterns. Three hydrides in $[Cu_{22}D_{16}H_3(NP_3)_4]^{3+}$ are due to the impurity of the borodeuteride source (the purity of $NaBD_4$ is 95%), which is unavoidable

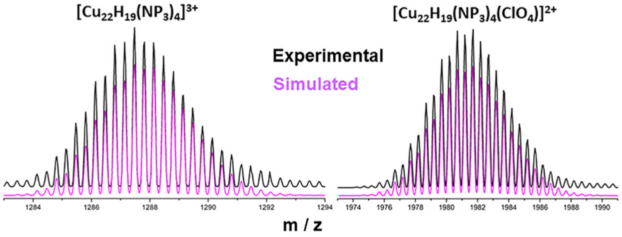

Fig. 2 HR ESI-MS spectra of dominant species $[Cu_{22}H_{19}(NP_3)_4]^{3+}$ and $[Cu_{22}H_{19}(NP_3)_4(ClO_4)]^{2+}$ along with simulated ones.

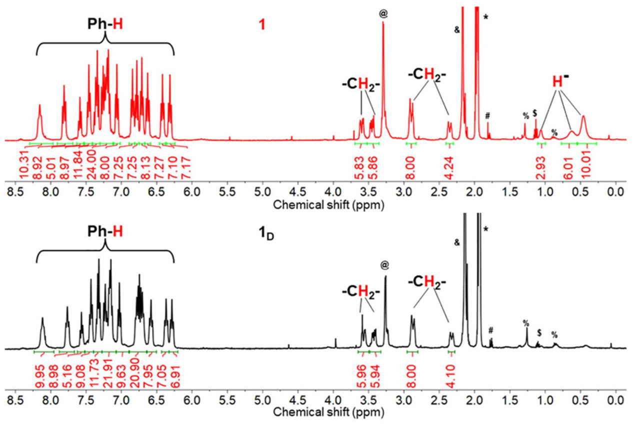

Fig. 3 ^1H NMR spectra of **1** and **1_D** in CD_3CN. The marked peaks correspond to CH_3OH (@), water (&), CH_3CN (*), and impurities in the solvent.

in polyhydrido copper clusters.[67] All these assigned species and the 19 mass difference between $[Cu_{22}H_{19}(NP_3)_4(ClO_4)]^{2+}$ and $[Cu_{22}D_{19}(NP_3)_4(ClO_4)]^{2+}$ confirm that cluster **1** has 19 hydride ligands (Fig. S8). Based on ESI-MS and SCXRD results, the total composition of **1** is proposed as $[Cu_{22}H_{19}(NP_3)_4(CH_3CN)_4]\cdot(ClO_4)_3$, and all the copper atoms are in the +1 state. The formulas assigned by ESI-MS are derived from the parent cluster **1^{3+}** with the loss of four MeCN molecules.

To further characterize the hydrides in **1**, ^1H NMR measurements were performed. The ^1H NMR spectrum of **1** features three broad peaks at 0.45, 0.62, and 1.06 ppm, which integrate for 10 H, 6 H and 3 H, respectively, and are assignable to 19 hydrides in different chemical environments. These peaks are completely missing in the ^1H NMR spectrum of **1_D** (Fig. 3 and Fig. S10), validating the assignment of hydrides. The peaks centred at 2.35 (4 H), 2.89 (8 H), 3.45 (6 H) and 3.60 (6 H) ppm in the spectrum of **1** are ascribed to 24 H of $-CH_2-$ moieties, while the peaks at 6.2–8.3 ppm correspond to 120 H of phenyl groups in ligands. Furthermore, the comparison of ^1H NMR spectra shows that the peaks of $-CH_2-$ and phenyl groups in **1** and **1_D** are almost consistent. In CD_3CN, the ^{31}P NMR spectrum of complex **1** exhibits three broad peaks at −3.44, −0.61, and 0.03 ppm, with an integration ratio of 1 : 1 : 1 (Fig. S11), suggesting that the twelve phosphine atoms in **1** are distributed into three distinct groups. Four phosphines are assigned to the terminal sites of the fused Cu_{22} polyhedron, while the remaining eight phosphines, located at the waist of the Cu_{22} framework, are further divided into two groups each of which is associated with one of the two Cu_{13} icosahedra.

The crystal structure, ESI-MS and ^1H NMR for cluster 2

Cluster **2** crystallizes in the trigonal $R\bar{3}c$ space group. X-ray diffraction study reveals that it consists of 20 Cu atoms, 4 NP_3, 4 coordinated Cl^- ions, 3 coordinated CH_3CN solvent molecules, and 3 ClO_4^- anions, indicating that the cation charge of cluster **2** would be +3 which is balanced by three ClO_4^- counterions. The skeleton of 20 Cu can be described as a centred Cu_{13} icosahedron covered by a cap-like Cu_7 moiety which consists of a Cu_6 hexagon (Cu6, Cu6i, Cu6ii, Cu7, Cu7i and Cu7ii) with nonplanar chair configuration and a top Cu atom (Cu_8) that is bonded to three interval Cu atoms in the hexagon and a terminal Cl^- ion with Cu–Cu and Cu–Cl distances of 2.528(1) and 2.183(2) Å respectively (Fig. 4). The *C*3 axis passes through the top Cu atom in the Cu_7 moiety and the centred Cu atom in the icosahedron. Besides the Cu–Cu bonding between a Cu_3 triangle (Cu5, Cu5i and Cu5ii) in the Cu_{13} icosahedron and the Cu_6 hexagon, three Cl^- ions perform as a μ_3-bridging mode to link the Cu_{13} and Cu_6 moieties (the Cu–Cl bond length range is 2.298(2)–2.956(1) Å). Furthermore, three NP_3 ligands perform in a tetradentate mode (N, P, P, P) to bind four Cu atoms of which three Cu atoms belong to the Cu_6 hexagon and one to the icosahedron. The fourth NP_3 ligand performs in a tridentate (P, P, P) mode to bind a triangular Cu_3 plane (Cu1, Cu1i and Cu1ii) of this icosahedron. The remaining three Cu atoms on the surface of Cu_{13} are coordinated by three MeCN solvent molecules. The structure of **2** can be seen as an evolution from **1** by losing two Cu^+ ions. The skeleton of 20 Cu can be also viewed as an interpenetrating structure of a centred Cu_{13} icosahedron and a twisted Cu_{10} tetrahedron which share four Cu atoms, along with a top Cu atom capping a face of this tetrahedron (Fig. S12).

The range of Cu–Cu distances in **2** is 2.455(4)–3.004(3) Å which is a little larger than that in cluster **1**. But the average Cu_{center}–Cu_{icos} and Cu–P distances are 2.583 Å (range: 2.465(2)–2.682(4) Å) and 2.248 Å (range: 2.230(2)–2.267(3) Å), respectively, which are comparable with those observed in cluster **1** and other reported Cu hydride clusters.[47,73–75] The average distance of Cu–N is 2.065 Å and the Cu–μ_3–Cl distances are 2.298 and 2.570 Å.[84]

By comparing the geometric parameters of NP_3 ligands, it is found that the bond angle of C–N–C is a significant mark for the (P, P, P) tridentate and the (N, P, P, P) tetradentate coordination modes (Scheme S1 and Table S2). The average bond angle of C–N–C is about 108° in the tetradentate coordination mode, but this value experiences a large range with the

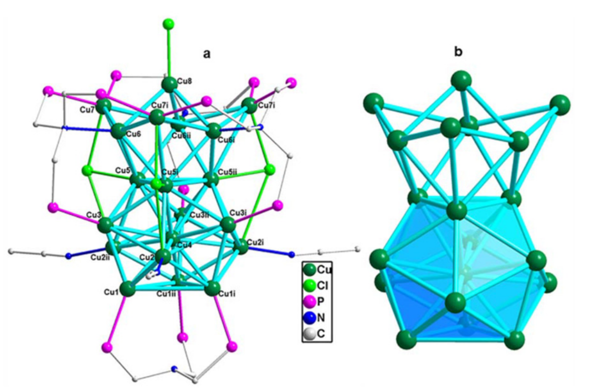

Fig. 4 The crystal structure of cluster **2** (a) and the skeleton of 20 Cu (b) in cluster **2**. All phenyl groups and hydrogen atoms are omitted for clarity. Symmetry codes: i = 1 − *y*, *x* − *y*, *z*; ii = 1 − *y* − *x*, 1 − *x*, *z*.

tridentate mode in different compounds. Moreover, the tridentate mode of NP_3 is appropriate to construct a triangular metal plane which exists in octahedral, icosahedral and tetrahedral structures, while the tetradentate coordination mode can match with complicated polyhedral structures.

To determine the number of hydrides in **2**, HR ESI-MS analyses of **2** and **2_D** are also performed (Fig. S13). The positive ESI-MS of **2** shows three characteristic signals at 1290.76 with a charge of +3 and 1953.67 and 1985.65 with a charge of +2, which match well respectively with the simulated isotopic patterns of $[Cu_{20}H_{13}(NP_3)_4Cl_4]^{3+}$, $[Cu_{20}H_{13}(NP_3)_4Cl_5]^{2+}$ and $[Cu_{20}H_{13}(NP_3)_4Cl_4(ClO_4)]^{2+}$ (Fig. 5). While the ESI-MS peaks of its deuteride analogue, **2_D**, at 1294.81 with a charge of +3 and 1959.70 and 1991.71 with a charge of +2 match well respectively with the simulated isotopic patterns of $[Cu_{20}D_{12}H(NP_3)_4Cl_4]^{3+}$, $[Cu_{20}D_{12}H(NP_3)_4Cl_5]^{2+}$ and $[Cu_{20}D_{12}H(NP_3)_4Cl_4(ClO_4)]^{2+}$ (Fig. S14). These formula assignments are validated by the good agreement between simulated and experimental isotopic patterns. All the species reveal the incorporation of 13 hydrides in **2** (Fig. S13). So the composition of **2** is proposed as $[Cu_{20}H_{13}Cl_4(CH_3CN)_3(NP_3)_4]\cdot(ClO_4)_3$. The formulas assigned by ESI-MS are derived from the loss of MeCN molecules from the parent cluster **2^{3+}**.

To further characterize the hydrides, the ^1H NMR spectra of **2** and **2_D** are compared in CD_3CN. The peaks centred at −0.50, −0.10 and 1.85 ppm for **2** are absent for **2_D**, showing that these peaks ascribed to H^- ions in **2** are replaced by D^- ions in **2_D** (Fig. 6). The peak integration of the ^1H NMR spectrum of **2** shows that 9 hydrides are equally distributed to three peaks at −0.50, −0.10 and 1.85 ppm, and four hydrides are overlapped with $-CH_2-$ in NP_3 at 3.37–3.99 ppm with one hydride at 3.37–3.66 ppm and three hydrides at 3.67–3.99 ppm. And these four overlapped hydride signals are also absent in the spectrum of **2_D**. To further determine quantitatively these hydrides in **2**, an internal standard reagent of 1,3,5-trioxane is used to perform ^1H NMR in $(CD_3)_2SO$. As shown in Fig. S15, the quantitative result is consistent with that of the peak integration. However, the peaks of $-CH_2-$ in $(CD_3)_2SO$ are not well resolved relative to those in CD_3CN (Fig. S16). Complex **2** features four broad resonances in its ^{31}P NMR spectrum in CD_3CN, centered respectively at −8.88, 0.15, 0.95 and 7.34 ppm with an integration ratio of 1 : 1 : 1 : 1 (Fig. S17), suggesting that the twelve phosphine atoms in **2** are divided into four groups. Three phosphines are ascribed to the NP_3 ligand with the (P, P, P) tridentate coordination mode, and another three phosphines from different NP_3 ligands with the (N, P, P, P) tetradentate mode attach to the icosahedron. The remaining six phosphines, distributed into two groups, coordinate to the Cu atoms at the cap-like Cu_7 moiety.

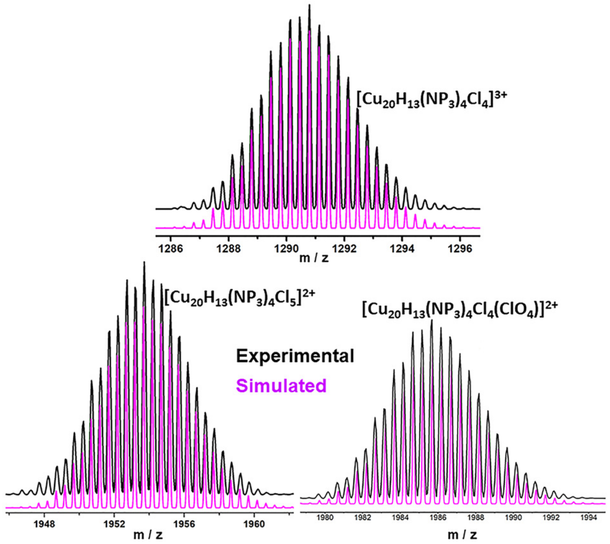

Fig. 5 HR ESI-MS spectra of characteristic species of $[Cu_{20}H_{13}(NP_3)_4Cl_4]^{3+}$, $[Cu_{20}H_{13}(NP_3)_4Cl_5]^{2+}$ and $[Cu_{20}H_{13}(NP_3)_4Cl_4(ClO_4)]^{2+}$ along with simulated ones.

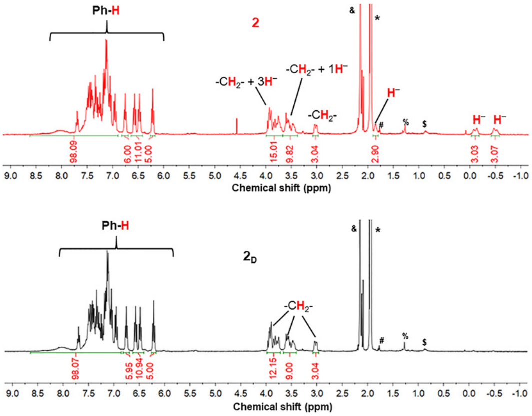

Fig. 6 ^1H NMR spectra of **2** and **2_D** in CD_3CN. The marked peaks correspond to water (&), CH_3CN (*), and impurities in the solvent.

The optimized results by DFT calculation

To ascertain the position of hydrides, several structural models consisting of hydrides for **1** and **2** are given based on the information from the crystal structural analysis, the observed hydride NMR chemical shifts and previously reported structures of hydride-containing copper clusters. Density functional theory (DFT) calculations are carried out for optimization until the default convergence limit is reached. It is worth mentioning that without any additional hydrogen atoms, the convergence cannot be carried out and the structure is cracked. The final optimized structure is nearly consistent with the experimental structure. The lowest energy structures for the corresponding clusters **1** and **2** are shown in Fig. 7 and S17.

There are six convergently optimized structures for cluster **1** (**1_{opa}**, **1_{opb}**, **1_{opc}**, **1_{opd}**, **1_{ope}** and **1_{opf}**), having nearly the same lowest energies and similar structures. To describe the positions of hydrides, the optimized structure of **1_{opa}** is used as an example. In optimized **1_{opa}**, one μ_6-hydride (H_a) as an interstitial locates at the center of the octahedral Cu_6 core in the fused icosahedra, and another 18 hydrides are distributed on

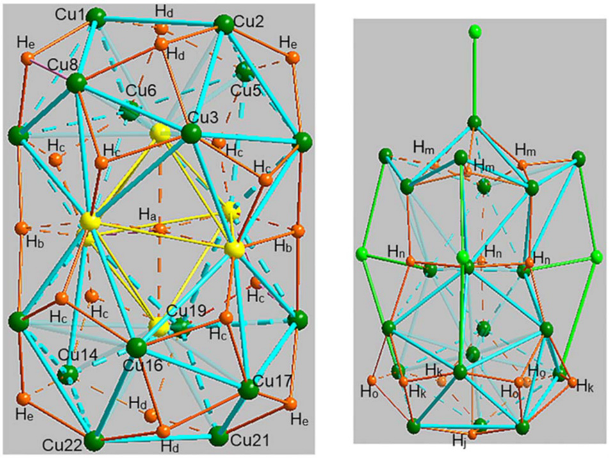

Fig. 7 Optimal hydride sites in $\mathbf{1_{opa}}$ (left) and **2** (right) based on DFT calculations. Colors: orange, H; green and yellow, Cu; and bright green, Cl.

the icosahedral surface. Among the 18 surface hydrides, two μ_4-hydrides (H_b) locate at the waist of the fused icosahedra to bridge respectively two fused Cu atoms and two differently icosahedral Cu atoms, each of 12 hydrides (H_c and H_e) performs as a μ_3 coordination mode capping a Cu_3 triangle, and each of the remaining four hydrides (H_d) locates above one irregular Cu_4 quadrangle and bridges three Cu atoms with a μ_3 coordination mode. The discrepancy among $\mathbf{1_{opa}}$–$\mathbf{1_{opf}}$ results from the drift of H_d positions as shown in Fig. S18. These drifts of H_d hydrides (also called "fluxional" hydrides) may result in the split of the ^1H NMR signal for H_d. So four H_d hydrides belong to two adjacent wide peaks at 0.25–0.85 ppm in the ^1H NMR spectrum of cluster **1**. The peak centred at 0.45 ppm contains 8 H_c and 2 H_d, while the peak centred at 0.62 ppm contains 4 H_e and 2 H_d. The H_a and 2 H_b are ascribed to the peak centred at 1.05 ppm.

In the optimized cluster **2**, seven hydrides adopt μ_4-H coordination modes and six hydrides adopt μ_3-H coordination modes. Each of three μ_4-H atoms (H_m) bridges the top Cu atom and three adjacent Cu atoms in the Cu_6 hexagon, while each of another three μ_4-H atoms (H_n) bridges one Cu atom from the Cu_6 hexagon and three Cu atoms of the icosahedron. The remaining one μ_4-H atom (H_j) bridges the central Cu atom in the icosahedron and three Cu atoms bound by the NP_3 ligand with a tridentate (P, P, P) mode. Moreover, each of the six μ_3-H atoms (H_k and H_o) bridges three triangular Cu atoms on the surface of the icosahedron. The hydride H_m is ascribed to the wide peak at −0.50 ppm, H_n at −0.10 ppm, H_k at 1.85 ppm, H_j at 3.37 to 3.66 ppm, and H_o at 3.67 to 3.99 ppm. The difference in the ^1H NMR peak locations between hydrides H_k and H_o may be ascribed to the anion effect in solution, though they have similar environments based on the crystal structure.

The Cu–Cu distances in X-ray and DFT structures for **1** and **2** are almost in good agreement and summarized in Table S3. And the Cu–H distances in **1** and **2** are comparable with those in previously reported Cu hydride clusters.[47,74]

The calculated band gaps based on the highest occupied molecular orbital (HOMO) and lowest unoccupied molecular orbital (LUMO) are 1.99 eV for **1** and 1.65 eV for **2**, which are smaller than their optical band gaps estimated by the extrapolation of the absorbance to the baseline.[45,67] The electronic charge densities of the frontier orbitals show that the nanocluster cores (including Cu and H) in **1** and **2** primarily contribute to the HOMOs and the LUMOs (Fig. S19 and S20).

Catalysis

To estimate the catalytic performances of clusters **1** and **2** with different structures, the reduction of 4-nitrophenol (4-NP) to 4-aminophenol (4-AP) by $NaBH_4$ in water is chosen as a model reaction (Scheme 2; the details of the catalytic experiment are provided in the SI). Clusters **1** and **2** do not dissolve in water, revealing that their catalytic reactions are heterogeneous. At a reaction temperature of 0 °C, the complete conversion of 4-NP catalyzed by cluster **2** takes 160 minutes, which is shorter than that catalyzed by cluster **1** (400 min) (Fig. 8). When the reaction is carried out at 25 °C, the time required for complete conversion of 4-NP catalyzed by cluster **2** is almost the same as that at 0 °C, which is still shorter than that catalyzed by cluster **1** at 25 °C (Fig. S21), showing that the temperature is not a strict requirement for the catalytic reaction. The time-dependent UV-visible spectra of 4-NP in an aqueous $NaBH_4$ solution remains unchanged in the absence of the nanocluster catalyst (Fig. S22), confirming that the nanocluster catalyst is necessary for the reduction of 4-NP.

Based on the change of UV-visible absorption of 4-NP with time at 0 °C and a wavelength of 400 nm, the calculated rate

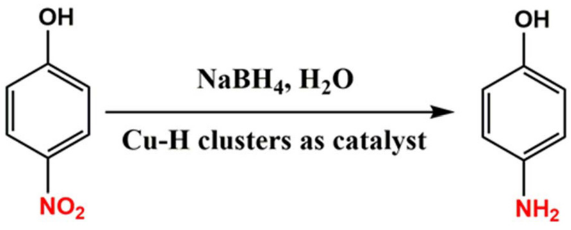

Scheme 2 A schematic diagram showing the catalytic reduction of 4-NP to 4-AP.

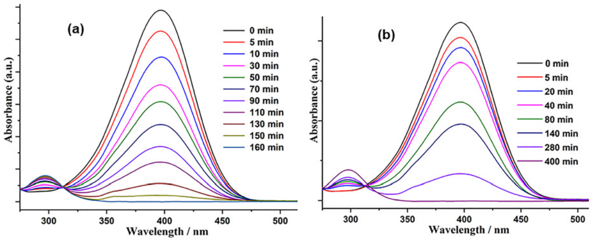

Fig. 8 UV -visible spectra showing the gradual reduction of 4-NP catalyzed by different catalysts: (a) cluster **2** and (b) cluster **1** in the presence of $NaBH_4$ at 0 °C. Catalytic experiment: 4-NP (9.45 mg, 2.27×10^{-2} M), $NaBH_4$ (257 mg, 6.8 mmol), cluster catalyst (3 mg) and 3 mL of H_2O.

constant for cluster **1** is $k = 0.0063\ \text{min}^{-1}$, but for cluster **2** the rate constants at high and low concentration of 4-NP are $k^h = 0.013\ \text{min}^{-1}$ and $k^l = 0.046\ \text{min}^{-1}$, respectively (Fig. S23). These rate constants indicate that the catalytic reactions are first-order processes. Their rate constants are lower than those of reported copper hydride nanoclusters (0.84 min^{-1} for $[(\text{TOP})\text{CuH}]_6$,[83] 0.5 min^{-1} for $\text{Cu}_{11}(\text{Tf-dpf})_6(\text{OAc})_2\text{H}_3)$,[84] but are comparable to that of $[\text{Cu}_{12}(\text{Tf-dpf})_6(\text{OAc})_2\text{H}_3]$ (0.007 min^{-1}).[84] The concentration-dependent rate constants for cluster **2** can be ascribed to the selective absorbance for 4-NP due to the non-equilibrium absorbing structure of cluster **2**. For a low concentration of 4-NP, the more active sites on the surface of cluster **2** are left for the cleavage of B–H in BH_4^-.

The catalytic performance of cluster **2** is better than that of cluster **1**, showing the existence of a structure effect. In addition to the different surface adsorbing ability of these two clusters, which influences their catalytic effect,[84,85] the possible transient dissociation of the hemilabile Cu–N bonds associating to NP_3 ligands in **2** could also produce active sites for effective catalytic reaction. However, the multidentate chelating ability of NP_3 still keeps the structure stable during the catalytic process. The recyclability of cluster **2** for the catalytic reduction of 4-NP is explored at 25 °C with a 160 min reaction time. After the twelfth cycle, the conversion of 4-NP is still 100% (Fig. S24), while the catalyst remains stable which is monitored by UV-visible spectroscopy of cluster **2** in MeCN (Fig. S25). Moreover, the reductions of 4-NP to 4-AP with NaBD_4 in place of NaBH_4 are also explored using clusters **1** and **2** as catalysts. After catalysis, the ESI-MS results show that no hydrides in **1** and **2** are replaced by D^- of BD_4^- (Fig. S26), which supports that the catalytic reaction happens on the surface of the clusters but the hydrides in the clusters are not involved in the catalysis.

Conclusions

In summary, we report the synthesis of two high-nuclearity Cu hydride nanoclusters of $\text{Cu}_{22}\text{H}_{19}$ and $\text{Cu}_{20}\text{H}_{13}$ and their deuteride analogues, $\text{Cu}_{22}\text{D}_{19}$ and $\text{Cu}_{20}\text{D}_{13}$, which are characterized by HR ESI-MS, ^{1}H NMR and single-crystal X-ray diffraction. DFT calculations support their compositions, structures and the sites of hydrides. The tetradentate NP_3 ligand acts to stabilize these structures with a tridentate mode (P, P, P) or a tetradentate mode (N, P, P, P). The small ionic ligands of H^- and Cl^- ions perform not only as bridging ligands but also as charge transport agents. However, the participation of Cl^- can also adjust the structure of Cu hydride nanoclusters due to the different sizes of H^- and Cl^- ions. Interestingly, the coordination of labile N atom can diversify structures and favor surface reactions. The structure of **2** can be seen as an evolution from **1** by losing two Cu^+ ions and due to the synergistic mediation of Cl^- ions and the NP_3 ligand. The catalytic performance of cluster 2 is better than that of cluster **1** for the reduction of 4-NP to 4-AP. This could result from the transient dissociation of hemilabile Cu–N bonds in **2** producing additional active sites for effective catalytic reaction, in addition to the different surface adsorption catalysis. Furthermore, cluster **2** exhibits different adsorption performances toward high and low concentrations of 4-NP.

Author contributions

The manuscript was written through contributions from all authors. All authors have given approval to the final version of the manuscript.

Conflicts of interest

The authors declare no competing financial interests.

Data availability statements

The data supporting this article have been included as part of the supplementary information (SI). Supplementary information: experimental details and methods, including synthesis, physical measurements, X-ray diffraction analysis of crystal structures, catalytic measurements and DFT calculations; and additional figures relating to crystal structures, UV-vis, XPS, ^{1}H NMR, and HR ESI-MS. See DOI: https://doi.org/10.1039/d5dt02358k.

CCDC 2241274 ($\text{Cu}_{20}\text{H}_{13}$) and 2241275 ($\text{Cu}_{22}\text{H}_{19}$) contain the supplementary crystallographic data for this paper.[86a,b]

Acknowledgements

We are grateful for financial support from the NSF of Guangxi Province in China (2023GXNSFDA026030 and 2019GXNSFGA245003) and the NSF of China (22165003 and 21861004). DFT calculations were provided by the High Performance Computing Center of Science and Engineering of Sichuan University of Science and Engineering.

References

1 I. Chakraborty and T. Pradeep, Atomically Precise Clusters of Noble Metals: Emerging Link between Atoms and Nanoparticles, *Chem. Rev.*, 2017, **117**, 8208–8271.
2 X. Kang, Y. Li, M. Zhu and R. Jin, Atomically precise alloy nanoclusters: syntheses, structures, and properties, *Chem. Soc. Rev.*, 2020, **49**, 6443–6514.
3 N. A. Sakthivel and A. Dass, Aromatic Thiolate-Protected Series of Gold Nanomolecules and a Contrary Structural Trend in Size Evolution, *Acc. Chem. Res.*, 2018, **51**, 1774–1783.
4 Q. Tang, G. Hu, V. Fung and D.-e. Jiang, Insights into Interfaces, Stability, Electronic Properties, and Catalytic

Activities of Atomically Precise Metal Nanoclusters from First Principles, *Acc. Chem. Res.*, 2018, **51**, 2793–2802.

5 V. K. Kulkarni, B. N. Khiarak, S. Takano, S. Malola, E. L. Albright, T. I. Levchenko, M. D. Aloisio, C.-T. Dinh, T. Tsukuda, H. Häkkinen and C. M. Crudden, N-Heterocyclic Carbene-Stabilized Hydrido Au$_{24}$ Nanoclusters: Synthesis, Structure, and Electrocatalytic Reduction of CO$_2$, *J. Am. Chem. Soc.*, 2022, **144**, 9000–9006.

6 Q.-Y. Wang, J. Wang, S. Wang, Z.-Y. Wang, M. Cao, C.-L. He, J.-Q. Yang, S.-Q. Zang and T. C. W. Mak, o-Carborane-Based and Atomically Precise Metal Clusters as Hypergolic Materials, *J. Am. Chem. Soc.*, 2020, **142**, 12010–12014.

7 Y. J. Kong, Z. P. Yan, S. Li, H. F. Su, K. Li, Y. X. Zheng and S. Q. Zang, Photoresponsive Propeller–like Chiral AIE Copper(I) Clusters, *Angew. Chem., Int. Ed.*, 2020, **59**, 5336–5340.

8 G. Soldan, M. A. Aljuhani, M. S. Bootharaju, L. G. AbdulHalim, M. R. Parida, A. H. Emwas, O. F. Mohammed and O. M. Bakr, Gold Doping of Silver Nanoclusters: A 26–Fold Enhancement in the Luminescence Quantum Yield, *Angew. Chem., Int. Ed.*, 2016, **55**, 5749–5753.

9 M. L. Fu, I. Issac, D. Fenske and O. Fuhr, Metal–Rich Copper Chalcogenide Clusters at the Border Between Molecule and Bulk Phase: The Structures of [Cu$_{93}$Se$_{42}$(SeC$_6$H$_4$SMe)$_9$(PPh$_3$)$_{18}$], [Cu$_{96}$Se$_{45}$(SeC$_6$H$_4$SMe)$_6$(PPh$_3$)$_{18}$], and [Cu$_{136}$S$_{56}$(SCH$_2$C$_4$H$_3$O)$_{24}$-(dpppt)$_{10}$], *Angew. Chem., Int. Ed.*, 2010, **49**, 6899–6903.

10 C.-L. Deng, B.-L. Han, Z.-Y. Liu, Z.-H. Pan, J. He, Y.-L. Li, Z.-L. Yang, G.-G. Luo, C.-H. Tung, D. Sun and L.-S. Zheng, Hierarchical Homochiral Assembly of Polyhedral Cage-Type Nanoclusters, *CCS Chem.*, 2024, **6**, 2537–2548.

11 B. Zhang, X. Tan, Z.-H. Zhang, C.-Y. Liu, F. Hu, H.-S. Hu, C. Chen and Q.-M. Wang, Atomically Precise Copper Nanoclusters with Cu-N Interfaces Toward Efficient CO$_2$-to-CH$_4$ Electrocatalysis, *CCS Chem.*, 2025, DOI: 10.31635/ccschem.025.202505606.

12 T. Jia, Z.-J. Guan, C. Zhang, X.-Z. Zhu, Y.-X. Chen, Q. Zhang, Y. Yang and D. Sun, Eight-Electron Superatomic Cu$_{31}$ Nanocluster with Chiral Kernel and NIR-II Emission, *J. Am. Chem. Soc.*, 2023, **145**, 10355–10363.

13 H. Zhao, C. Zhang, B. Han, Z. Wang, Y. Liu, Q. Xue, C.-H. Tung and D. Sun, Assembly of Air-stable Copper(I) Alkynide Nanoclusters Assisted by Tripodal Polydentate Phosphoramide Ligands, *Nat. Synth.*, 2024, **3**, 517–526.

14 N. A. Sakthivel, S. Theivendran, V. Ganeshraj, A. G. Oliver and A. Dass, Crystal Structure of Faradaurate-279: Au$_{279}$(SPh^{t}Bu)$_{84}$ Plasmonic Nanocrystal Molecules, *J. Am. Chem. Soc.*, 2017, **139**, 15450–15459.

15 M.-X. Ma, X.-L. Ma, G.-M. Liang, X.-T. Shen, Q.-L. Ni, L.-C. Gui, X.-J. Wang, S.-Y. Huang and S.-M. Li, A Nanocluster [Ag$_{307}$Cl$_{62}$(SPh-^{t}Bu)$_{110}$]: Chloride Intercalation, Specific Electronic State, and Superstability, *J. Am. Chem. Soc.*, 2021, **143**, 13731–13737.

16 H. Y. Yang, Y. Wang, X. Chen, X. J. Zhao, L. Gu, H. Q. Huang, J. Z. Yan, C. F. Xu, G. Li, J. C. Wu, A. J. Edwards, B. Dittrich, Z. C. Tang, D. D. Wang, L. Lehtovaara, H. Häkkinen and N. F. Zheng, Plasmonic Twinned Silver Nanoparticles with Molecular Precision, *Nat. Commun.*, 2016, **7**, 12809.

17 Y. Song, Y. Li, H. Li, F. Ke, J. Xiang, C. Zhou, P. Li, M. Zhu and R. Jin, Atomically Resolved Au$_{52}$Cu$_{72}$(SR)$_{55}$ Nanoalloy Reveals Marks Decahedron Truncation and Penrose Tiling Surface, *Nat. Commun.*, 2020, **11**, 478.

18 X.-T. Shen, X.-L. Ma, Q.-L. Ni, M.-X. Ma, L.-C. Gui, C. Hou, R.-B. Hou and X.-J. Wang, [Ag$_{15}$(N-triphos)$_4$(Cl$_4$)](NO$_3$)$_3$: a Stable Ag–P Superatom with Eight Electrons (N-triphos = tris((diphenyl-phosphino)methyl)amine), *Nanoscale*, 2018, **10**, 515–519.

19 X. Ma, Y. Bai, Y. Song, Q. Li, Y. Lv, H. Zhang, H. Yu and M. Zhu, Rhombicuboctahedral Ag$_{100}$: Four–Layered Octahedral Silver Nanocluster Adopting the Russian Nesting Doll Model, *Angew. Chem., Int. Ed.*, 2020, **59**, 17234–17238.

20 F. Hu, J. J. Li, Z. J. Guan, S. F. Yuan and Q. M. Wang, Formation of an Alkynyl–Protected Ag$_{112}$ Silver Nanocluster as Promoted by Chloride Released In Situ from CH$_2$Cl$_2$, *Angew. Chem., Int. Ed.*, 2020, **59**, 5312–5315.

21 J. Y. Liu, F. Alkan, Z. Wang, Z. Y. Zhang, M. Kurmoo, Z. Yan, Q. Q. Zhao, C. M. Aikens, C. H. Tung and D. Sun, Different Silver Nanoparticles in One Crystal: Ag$_{210}$(^{i}PrPhS)$_{71}$(Ph$_3$P)$_5$Cl and Ag$_{211}$(^{i}PrPhS)$_{71}$(Ph$_3$P)$_6$Cl, *Angew. Chem., Int. Ed.*, 2019, **58**, 195–199.

22 M. Diecke, C. Schrenk and A. Schnepf, Synthesis and Characterization of the Highly Unstable Metalloid Cluster Ag$_{64}$(P^{n}Bu$_3$)$_{16}$Cl$_6$, *Angew. Chem., Int. Ed.*, 2020, **59**, 14418–14422.

23 T. Higaki, M. Zhou, K. J. Lambright, K. Kirschbaum, M. Y. Sfeir and R. Jin, Sharp Transition from Nonmetallic Au$_{246}$ to Metallic Au$_{279}$ with Nascent Surface Plasmon Resonance, *J. Am. Chem. Soc.*, 2018, **140**, 5691–5695.

24 Z. Gan, J. Chen, J. Wang, C. Wang, M.-B. Li, C. Yao, S. Zhuang, A. Xu, L. Li and Z. Wu, The Fourth Crystallographic Closest Packing Unveiled in the Gold Nanocluster Crystal, *Nat. Commun.*, 2017, **8**, 14739.

25 C. Zeng, Y. Chen, K. Kirschbaum, K. J. Lambright and R. Jin, Emergence of Hierarchical Structural Complexities in Nanoparticles and Their Assembly, *Science*, 2016, **354**, 1580–1584.

26 H. Yoshida, M. Ehara, U. D. Priyakumar, T. Kawai and T. Nakashima, Enantioseparation and Chiral Induction in Ag$_{29}$ Nanoclusters with Intrinsic Chirality, *Chem. Sci.*, 2020, **11**, 2394–2400.

27 N. Xia, J. Xing, D. Peng, S. Ji, J. Zha, N. Yan, Y. Su, X. Jiang, Z. Zeng, J. Zhao and Z. Wu, Assembly-induced Spin Transfer and Distance-dependent Spin Coupling in Atomically Precise AgCu Nanoclusters, *Nat. Commun.*, 2022, **13**, 5934.

28 X. Kang and M. Zhu, Intra-cluster Growth Meets Inter-cluster Assembly: The Molecular and Supramolecular Chemistry of Atomically Precise Nanoclusters, *Coord. Chem. Rev.*, 2019, **394**, 1–38.

29 J.-Q. Wang, S. Shi, R.-L. He, S.-F. Yuan, G.-Y. Yang, G.-J. Liang and Q.-M. Wang, Total Structure Determination of the Largest Alkynyl-Protected fcc Gold Nanocluster Au_{110} and the Study on Its Ultrafast Excited-State Dynamics, *J. Am. Chem. Soc.*, 2020, **142**, 18086–18092.

30 H. Qian, W. T. Eckenhoff, Y. Zhu, T. Pintauer and R. Jin, Total Structure Determination of Thiolate-Protected Au_{38} Nanoparticles, *J. Am. Chem. Soc.*, 2010, **132**, 8280–8281.

31 D.-e. Jiang, M. L. Tiago, W. Luo and S. Dai, The "Staple" Motif: A Key to Stability of Thiolate-Protected Gold Nanoclusters, *J. Am. Chem. Soc.*, 2008, **130**, 2777–2779.

32 S. Zhuang, L. Liao, Y. Zhao, J. Yuan, C. Yao, X. Liu, J. Li, H. Deng, J. Yang and Z. Wu, Is the Kernel–staples Match a Key–lock Match?, *Chem. Sci.*, 2018, **9**, 2437–2442.

33 A. J. Edwards, R. S. Dhayal, P. K. Liao, J. H. Liao, M. H. Chiang, R. O. Piltz, S. Kahlal, J. Y. Saillard and C. W. Liu, Chinese Puzzle Molecule: A 15 Hydride, 28Copper Atom Nanoball, *Angew. Chem., Int. Ed.*, 2014, **53**, 7214–7218.

34 F. Tian and R. Chen, $Ag_{18}(\mu_8\text{-}S)(p\text{-}TBBT)_{16}(PPh_3)_8$: Symmetry Breaking Induced by the Core to Generate Chirality, *Chem. Commun.*, 2020, **56**, 2719–2722.

35 A. Baghdasaryan and T. Bürgi, Copper Nanoclusters: Designed Synthesis, Structural Diversity, and Multiplatform Applications, *Nanoscale*, 2021, **13**, 6283–6340.

36 A. J. Jordan, G. Lalic and J. P. Sadighi, Coinage Metal Hydrides: Synthesis, Characterization, and Reactivity, *Chem. Rev.*, 2016, **116**, 8318–8372.

37 S. Shahsavari, S. Hadian-Ghazvini, F. Hooriabad Saboor, I. Menbari Oskouie, M. Hasany, A. Simchi and A. L. Rogach, Ligand Functionalized Copper Nanoclusters for Versatile Applications in Catalysis, Sensing, Bioimaging, and Optoelectronics, *Mater. Chem. Front.*, 2019, **3**, 2326–2356.

38 R. S. Dhayal, W. E. van Zyl and C. W. Liu, Copper Hydride Clusters in Energy Storage and Conversion, *Dalton Trans.*, 2019, **48**, 3531–3538.

39 R. S. Dhayal, W. E. van Zyl and C. W. Liu, Polyhydrido Copper Clusters: Synthetic Advances, Structural Diversity, and Nanocluster-to-Nanoparticle Conversion, *Acc. Chem. Res.*, 2015, **49**, 86–95.

40 C. Sun, B. K. Teo, C. Deng, J. Lin, G.-G. Luo, C.-H. Tung and D. Sun, Hydrido-coinage-metal Clusters: Rational Design, Synthetic Protocols and Structural Characteristics, *Coord. Chem. Rev.*, 2021, **427**, 213576.

41 D. A. Ekanayake, A. Chakraborty, J. A. Krause and H. Guan, Hydrogenation Reactions Catalyzed by $HN(CH_2CH_2PR_2)_2$-ligated Copper Complexes, *Inorg. Chem. Front.*, 2021, **8**, 4634–4649.

42 R. S. Dhayal, J.-H. Liao, Y.-R. Lin, P.-K. Liao, S. Kahlal, J.-Y. Saillard and C. W. Liu, A Nanospheric Polyhydrido Copper Cluster of Elongated Triangular Orthobicupola Array: Liberation of H_2 from Solar Energy, *J. Am. Chem. Soc.*, 2013, **135**, 4704–4707.

43 R. P. B. Silalahi, Q. Wang, J. H. Liao, T. H. Chiu, Y. Y. Wu, X. Wang, S. Kahlal, J. Y. Saillard and C. W. Liu, Reactivities of Interstitial Hydrides in a Cu_{11} Template: En Route to Bimetallic Clusters, *Angew. Chem., Int. Ed.*, 2022, **61**, e202113266.

44 R. S. Dhayal, J. H. Liao, X. Wang, Y. C. Liu, M. H. Chiang, S. Kahlal, J. Y. Saillard and C. W. Liu, Diselenophosphate-Induced Conversion of an Achiral $[Cu_{20}H_{11}\{S_2P(O\mathit{i}Pr)_2\}_9]$ into a Chiral $[Cu_{20}H_{11}\{Se_2P(O\mathit{i}Pr)_2\}_9]$ Polyhydrido Nanocluster, *Angew. Chem., Int. Ed.*, 2015, **54**, 13604–13608.

45 R.-W. Huang, J. Yin, C. Dong, P. Maity, M. N. Hedhili, S. Nematulloev, B. Alamer, A. Ghosh, O. F. Mohammed and O. M. Bakr, $[Cu_{23}(PhSe)_{16}(Ph_3P)_8(H)_6]\cdot BF_4$: Atomic-Level Insights into Cuboidal Polyhydrido Copper Nanoclusters and Their Quasi-simple Cubic Self-Assembly, *ACS Mater. Lett.*, 2021, **3**, 90–99.

46 C. Sun, N. Mammen, S. Kaappa, P. Yuan, G. Deng, C. Zhao, J. Yan, S. Malola, K. Honkala, H. Häkkinen, B. K. Teo and N. Zheng, Atomically Precise, Thiolated Copper–Hydride Nanoclusters as Single-Site Hydrogenation Catalysts for Ketones in Mild Conditions, *ACS Nano*, 2019, **13**, 5975–5986.

47 T.-A. D. Nguyen, Z. R. Jones, B. R. Goldsmith, W. R. Buratto, G. Wu, S. L. Scott and T. W. Hayton, A Cu_{25} Nanocluster with Partial Cu(0) Character, *J. Am. Chem. Soc.*, 2015, **137**, 13319–13324.

48 S. Li, X. Yan, J. Tang, D. Cao, X. Sun, G. Tian, X. Tang, H. Guo, Q. Wu, J. Sun, J. He and H. Shen, Cu_{26} Nanoclusters with Quintuple Ligand Shells for CO_2 Electrocatalytic Reduction, *Chem. Mater.*, 2023, **35**, 6123–6132.

49 Y. Bao, X. Wu, B. Yin, X. Kang, Z. Lin, H. Deng, H. Yu, S. Jin, S. Chen and M. Zhu, Structured Copper-hydride Nanoclusters Provide Insight into the Surface-vacancy-defect to Non-defect Structural Evolution, *Chem. Sci.*, 2022, **13**, 14357–14365.

50 S. Nematulloev, A. Sagadevan, B. Alamer, A. Shkurenko, R. Huang, J. Yin, C. Dong, P. Yuan, K. E. Yorov, A. A. Karluk, W. J. Mir, B. E. Hasanov, M. Nejib Hedhili, N. M. Halappa, M. Eddaoudi, O. F. Mohammed, M. Rueping and O. M. Bakr, Atomically Precise Defective Copper Nanocluster Catalysts for Highly Selective C–C Cross–Coupling Reactions, *Angew. Chem., Int. Ed.*, 2023, **62**, e202303572.

51 Q.-L. Guo, B.-L. Han, C.-F. Sun, Z. Wang, Y. Tao, J.-Q. Lin, G.-G. Luo, C.-H. Tung and D. Sun, Observation of a Bcc-like Framework in Polyhydrido Copper Nanoclusters, *Nanoscale*, 2021, **13**, 19642–19649.

52 X. Liu, H. Shen, Y. Gao, G. Deng, H. Deng, Y.-Z. Han, B. K. Teo and N. Zheng, $Cu_{28}H_{20}$: a Peculiar Chiral Nanocluster with an Exposed Cu Atom and 13 Surface Hydrides, *Chem. Commun.*, 2022, **58**, 7670–7673.

53 T.-A. D. Nguyen, Z. R. Jones, D. F. Leto, G. Wu, S. L. Scott and T. W. Hayton, Ligand-Exchange-Induced Growth of an Atomically Precise Cu_{29} Nanocluster from a Smaller Cluster, *Chem. Mater.*, 2016, **28**, 8385–8390.

54 S. K. Barik, S. C. Huo, C. Y. Wu, T. H. Chiu, J. H. Liao, X. Wang, S. Kahlal, J. Y. Saillard and C. W. Liu, Polyhydrido Copper Nanoclusters with a Hollow Icosahedral Core: [$Cu_{30}H_{18}\{E_2P(OR)_2\}_{12}$] (E=S or Se; R=nPr, iPr or iBu), *Chem. – Eur. J.*, 2020, **26**, 10471–10479.

55 H. Shen, L. Wang, O. López-Estrada, C. Hu, Q. Wu, D. Cao, S. Malola, B. K. Teo, H. Häkkinen and N. Zheng, Copper-hydride Nanoclusters with Enhanced Stability by N-heterocyclic Carbenes, *Nano Res.*, 2021, **14**, 3303–3308.

56 S. Lee, M. S. Bootharaju, G. Deng, S. Malola, W. Baek, H. Häkkinen, N. Zheng and T. Hyeon, [$Cu_{32}(PET)_{24}H_8Cl_2$] (PPh_4)$_2$: A Copper Hydride Nanocluster with a Bisquare Antiprismatic Core, *J. Am. Chem. Soc.*, 2020, **142**, 13974–13981.

57 R. S. Dhayal, J. H. Liao, S. Kahlal, X. Wang, Y. C. Liu, M. H. Chiang, W. E. van Zyl, J. Y. Saillard and C. W. Liu, [$Cu_{32}(H)_{20}\{S_2P(O\textit{i}Pr)_2\}_{12}$]: The Largest Number of Hydrides Recorded in a Molecular Nanocluster by Neutron Diffraction, *Chem. – Eur. J.*, 2015, **21**, 8369–8374.

58 C. Dong, R.-W. Huang, C. Chen, J. Chen, S. Nematulloev, X. Guo, A. Ghosh, B. Alamer, M. N. Hedhili, T. T. Isimjan, Y. Han, O. F. Mohammed and O. M. Bakr, [$Cu_{36}H_{10}(PET)_{24}(PPh_3)_6Cl_2$] Reveals Surface Vacancy Defects in Ligand-Stabilized Metal Nanoclusters, *J. Am. Chem. Soc.*, 2021, **143**, 11026–11035.

59 J. Zhou, W.-W. Zhan, Y. Li, X.-R. Gao, C. Zhang, D. Sun and Y. Yang, Hydride-Richest Molecular Complex: Ligand-Length Facilitated $Cu_{40}H_{38}$ Nanoclusters Exhibiting High Catalytic Performance for Selective Hydrogenation, *Angew. Chem., Int. Ed.*, 2025, **64**, e202504671.

60 H. Zhou, T. Duan, Z. Lin, T. Yang, H. Deng, S. Jin, Y. Pei and M. Zhu, Total Structure, Structural Transformation and Catalytic Hydrogenation of [$Cu_{41}(SC_6H_3F_2)_{15}Cl_3(P(PhF)_3)_6(H)_{25}$]$_2$– Constructed from Twisted Cu_{13} Units, *Adv. Sci.*, 2023, **11**, 2307085.

61 P. Yuan, R. Chen, X. Zhang, F. Chen, J. Yan, C. Sun, D. Ou, J. Peng, S. Lin, Z. Tang, B. K. Teo, L. S. Zheng and N. Zheng, Ether–Soluble Cu_{53} Nanoclusters as an Effective Precursor of High–Quality CuI Films for Optoelectronic Applications, *Angew. Chem., Int. Ed.*, 2019, **58**, 835–839.

62 G. G. Luo, Z. H. Pan, B. L. Han, G. L. Dong, C. L. Deng, M. Azam, Y. W. Tao, J. He, C. F. Sun and D. Sun, Total Structure, Electronic Structure and Catalytic Hydrogenation Activity of Metal–Deficient Chiral Polyhydride Cu_{57} Nanoclusters, *Angew. Chem., Int. Ed.*, 2023, **62**, e202306849.

63 C. Dong, R. W. Huang, A. Sagadevan, P. Yuan, L. Gutiérrez–Arzaluz, A. Ghosh, S. Nematulloev, B. Alamer, O. F. Mohammed, I. Hussain, M. Rueping and O. M. Bakr, Isostructural Nanocluster Manipulation Reveals Pivotal Role of One Surface Atom in Click Chemistry, *Angew. Chem., Int. Ed.*, 2023, **62**, e202307140.

64 S. Biswas, S. Hossian, T. Kosaka, J. Sakai, D. Arima, Y. Niihori, M. Mitsui, D.-e. Jiang, S. Das, S. Wang and Y. Negishi, Nested Keplerian Architecture of [$Cu_{58}H_{20}(SPr)_{36}(PPh_3)_8$]$^{2+}$ Nanoclusters, *Chem. Commun.*, 2023, **59**, 9336–9339.

65 A. Ghosh, R.-W. Huang, B. Alamer, E. Abou-Hamad, M. N. Hedhili, O. F. Mohammed and O. M. Bakr, [$Cu_{61}(StBu)_{26}S_6Cl_6H_{14}$]$^+$: A Core–Shell Superatom Nanocluster with a Quasi-J36 Cu_{19} Core and an "18-Crown-6" Metal-Sulfide-like Stabilizing Belt, *ACS Mater. Lett.*, 2019, **1**, 297–302.

66 H.-N. Qin, M.-W. He, J. Wang, H.-Y. Li, Z.-Y. Wang, S.-Q. Zang and T. C. W. Mak, Thiacalix[4]arene Etching of an Anisotropic $Cu_{70}H_{22}$ Intermediate for Accessing Robust Modularly Assembled Copper Nanoclusters, *J. Am. Chem. Soc.*, 2024, **146**, 3545–3552.

67 R.-W. Huang, J. Yin, C. Dong, A. Ghosh, M. J. Alhilaly, X. Dong, M. N. Hedhili, E. Abou-Hamad, B. Alamer, S. Nematulloev, Y. Han, O. F. Mohammed and O. M. Bakr, [$Cu_{81}(PhS)_{46}(tBuNH_2)_{10}(H)_{32}$]$^{3+}$ Reveals the Coexistence of Large Planar Cores and Hemispherical Shells in High-Nuclearity Copper Nanoclusters, *J. Am. Chem. Soc.*, 2020, **142**, 8696–8705.

68 T. Tanase, K. Nakamae, Y. Ura and T. Nakajima, Fine Tunable Metal Assemblies Constrained by Multidentate Phosphine Ligands, *Coord. Chem. Rev.*, 2022, **466**, 214581.

69 T. Nakajima, K. Nakamae, Y. Ura and T. Tanase, Multinuclear Copper Hydride Complexes Supported by Polyphosphine Ligands, *Eur. J. Inorg. Chem.*, 2020, **2020**, 2211–2226.

70 C. M. Zall, J. C. Linehan and A. M. Appel, Triphosphine-Ligated Copper Hydrides for CO_2 Hydrogenation: Structure, Reactivity, and Thermodynamic Studies, *J. Am. Chem. Soc.*, 2016, **138**, 9968–9977.

71 S. Nematulloev, R. W. Huang, J. Yin, A. Shkurenko, C. Dong, A. Ghosh, B. Alamer, R. Naphade, M. N. Hedhili, P. Maity, M. Eddaoudi, O. F. Mohammed and O. M. Bakr, [$Cu_{15}(PPh_3)_6(PET)_{13}$]$^{2+}$: a Copper Nanocluster with Crystallization Enhanced Photoluminescence, *Small*, 2021, **17**, 2006839.

72 M. R. Churchill, S. A. Bezman, J. A. Osborn and J. Wormald, Synthesis and Molecular Geometry of Hexameric Triphenyl-phosphinocopper(I) Hydride and the Crystal Structure of $H_6Cu_6(PPh_3)_6$. $HCONMe_2$ [Hexameric Triphenylphosphino Copper(I) Hydride Dimethylformamide], *Inorg. Chem.*, 1972, **11**, 1818–1825.

73 T. A. D. Nguyen, B. R. Goldsmith, H. T. Zaman, G. Wu, B. Peters and T. W. Hayton, Synthesis and Characterization of a Cu_{14} Hydride Cluster Supported by Neutral Donor Ligands, *Chem. – Eur. J.*, 2015, **21**, 5341–5344.

74 K. Nakamae, T. Nakajima, Y. Ura, Y. Kitagawa and T. Tanase, Facially Dispersed Polyhydride Cu_9 and Cu_{16} Clusters Comprising Apex–Truncated Supertetrahedral and Square–Face–Capped Cuboctahedral Copper Frameworks, *Angew. Chem., Int. Ed.*, 2020, **59**, 2262–2267.

75 J. Li, H. Z. Ma, G. E. Reid, A. J. Edwards, Y. Hong, J. M. White, R. J. Mulder and R. A. J. O'Hair, Synthesis and X-Ray Crystallographic Characterisation of Frustum-Shaped Ligated [$Cu_{18}H_{16}(DPPE)_6$]$^{2+}$ and [$Cu_{16}H_{14}(DPPA)_6$]$^{2+}$ Nanoclusters and Studies on Their H_2 Evolution Reactions, *Chem. – Eur. J.*, 2018, **24**, 2070–2074.

76 Q. L. Ni, F. Zhang, T. H. Huang, X. P. Wu, X. J. Wang, G. M. Liang and K. G. Yang, Octahedral and Cyclic [Ag_6] Cluster Cores Stabilized by {$Ag_3(Spz)_3$(N-triphos)$_3$} Motifs [HSpz = Pyrazine-2-thiolate, N-triphos = Tris((diphenylphosphanyl)methyl)-amine]: Ag⋯Ag Interactions, *Z. Anorg. Allg. Chem.*, 2015, **641**, 2664–2669.

77 R. Jin, C. Liu, S. Zhao, A. Das, H. Xing, C. Gayathri, Y. Xing, N. L. Rosi and R. Jin, Tri-icosahedral Gold Nanocluster $[Au_{37}(PPh_3)_{10}(SC_2H_4Ph)_{10}X_2]^+$: Linear Assembly of Icosahedral Building Blocks, *ACS Nano*, 2015, **9**, 8530–8536.

78 T.-H. Chiu, J.-H. Liao, F. Gam, I. Chantrenne, S. Kahlal, J.-Y. Saillard and C. W. Liu, Homoleptic Platinum/Silver Superatoms Protected by Dithiolates: Linear Assemblies of Two and Three Centered Icosahedra Isolobal to Ne_2 and I_3^-, *J. Am. Chem. Soc.*, 2019, **141**, 12957–12961.

79 Y. Song, F. Fu, J. Zhang, J. Chai, X. Kang, P. Li, S. Li, H. Zhou and M. Zhu, The Magic Au60 Nanocluster: A New Cluster–Assembled Material with Five Au_{13} Building Blocks, *Angew. Chem., Int. Ed.*, 2015, **54**, 8430–8434.

80 B. K. Teo, H. Zhang and X. Shi, a Modular Approach to Large Metal Clusters. Structural Characterization of a 38-atom Cluster [(p-Tol$_3$P)$_{12}$Au$_{18}$Ag$_{20}$Cl$_{14}$] Based on Vertex-sharing Triicosahedra, *J. Am. Chem. Soc.*, 1990, **112**, 8552–8562.

81 C. Xu, Y. Zhou, J. Yi, D. Li, L. Shi and L. Cheng, Tri- and Tetra-superatomic Molecules in Ligand-Protected Face-Fused Icosahedral (M@Au_{12})n (M = Au, Pt, Ir, and Os, and n = 3 and 4) Clusters, *J. Phys. Chem. Lett.*, 2022, **13**, 1931–1939.

82 H. Yang, Y. Wang, A. J. Edwards, J. Yan and N. Zheng, High-yield Synthesis and Crystal Structure of a Green Au_{30}cluster Co-capped by Thiolate and Sulfide, *Chem. Commun.*, 2014, **50**, 14325–14327.

83 X. Zheng, Y. Liu, W. Ma, Y. Su and Y. Wang, The structure–activity Relationship of Copper Hydride Nanoclusters in Hydrogenation and Reduction Reactions, *Nanoscale Adv.*, 2024, **6**, 1374–1379.

84 C.-Y. Liu, S.-F. Yuan, S. Wang, Z.-J. Guan, D.-e. Jiang and Q.-M. Wang, Structural Transformation and Catalytic Hydrogenation Activity of Amidinate-protected Copper Hydride Clusters, *Nat. Commun.*, 2022, **13**, 2082.

85 S. M. Ansar and C. L. Kitchens, Impact of Gold Nanoparticle Stabilizing Ligands on the Colloidal Catalytic Reduction of 4-Nitrophenol, *ACS Catal.*, 2016, **6**, 5553–5560.

86 (*a*) CCDC 2241274: Experimental Crystal Structure Determination, 2025, DOI: 10.5517/ccdc.csd.cc2f7753; (*b*) CCDC 2241275: Experimental Crystal Structure Determination, 2025, DOI: 10.5517/ccdc.csd.cc2f7764.